MDPI

Article

Synthetic BiOBr/Bi$_2$S$_3$/CdS Crystalline Material and Its Degradation of Dye under Visible Light

Yunhan Jin [1], Zhe Xing [1,2], Yinhui Li [1], Jian Han [1], Heike Lorenz [3] and Jianxin Chen [1,4,*]

[1] School of Chemical Engineering and Technology, Hebei University of Technology, Tianjin 300130, China; q724778596@126.com (Y.J.); xingzhe1995@126.com (Z.X.); liyinhui@hebut.edu.cn (Y.L.); superhj@hebut.edu.cn (J.H.)
[2] CenerTech Tianjin Chemical Research and Design Insitute Co. Ltd., Tianjin 300131, China
[3] Max Planck Institute for Dynamics of Complex Technical Systems, D-39106 Magdeburg, Germany; lorenz@mpi-magdeburg.mpg.de
[4] National-Local Joint Engineering Laboratory for Energy Conservation in Chemical Process Integration and Resources Utilization, Hebei University of Technology, Tianjin 300130, China
* Correspondence: chjx2000@126.com

Abstract: Constructing heterojunction has attracted widespread concerns in photocatalysis research. BiOBr/Bi$_2$S$_3$/CdS composite material with a sea urchin shape was directly obtained by first synthesizing BiOBr microspheres. The morphology, structure and composition of the composite material were characterized by XRD, EDX, SEM and XPS. Dye degradation experiments showed that 83.3% of methylene blue removal was achieved after 2 h of visible light irradiation. The reaction rate under optimal conditions was 0.014 min^{-1} and the photocatalytic degradation process follows a pseudo-first-order kinetic model. Based on the EPR test results, the main active species involved in the reaction were $\bullet O_2{}^-$ and h$^+$. The conduction band and valence band edge potential calculations confirmed the key role of CdS in the production of $\bullet O_2{}^-$.

1. Introduction

As an important part of colorants, dyes are widely used in cosmetics, food, paper, pharmaceuticals, plastics, textile and leather industries and consume a lot of water [1–3]. The discharge of organic pollutants such as dyes into freshwater resources often causes a series of serious health risks. The carcinogenicity, teratogenicity and reproductive toxicity of dye wastewater directly threaten aquatic organisms and cause serious water pollution [4,5]. Therefore, the dye concentration in wastewater must be reduced below the safety limit before being released into the environment. However, it is not easy to treat dye-containing wastewater. Due to their high light and thermal stability, dyes are difficult to be biodegraded in natural waters [6,7]. The stability of dyes against soaps, oxidants, detergents, biological and chemical reagents makes them difficult to mineralize [8]. Therefore, the treatment of dye wastewater has become a major problem in industrial wastewater treatment, and it is essential to develop more effective, green and economic dye wastewater treatment processes.

Photocatalytic semiconductor materials have received extensive attention due to their great potential in degrading organic pollutants [9–11]. As one of the best types of photocatalysts, Bi-based photocatalysts have shown wide application prospects in various fields including wastewater remediation. Among Bi-based photocatalysts, bismuth oxybromide (BiOBr) has become one of the most popular semiconductor materials for photocatalysis due to its good chemical durability and excellent photocatalytic activity under visible light irradiation [12,13]. BiOBr is a novel two-dimensional material with a layered crystal structure. [Bi$_2$O$_2$]$^{2+}$ is sandwiched between halogen ions, and the static internal electric field (IEF) is generated by the electrostatic potential difference between these ions. The

static IEF in BiOBr can effectively split and transfer electrons and holes produced by light [14,15]. Pure BiOBr limits its photocatalytic efficiency due to its wide band gap and rapid recombination of photo-generated carriers. Recently, some strategies to improve the photocatalytic activity of BiOBr have been implemented, especially by manufacturing BiOBr-based heterostructure composite materials [16–18]. These photocatalysts integrate the synergy between the components, which can enhance the visible light capture ability and photocatalytic activity of the material.

Bismuth sulfide (Bi_2S_3) is another Bi-based semiconductor. Because of its unique narrow band gap (about 1.4 eV) and photocarrier trapping effect, it was used in the photolysis of water to produce hydrogen, and solar energy [19]. At the same time, since the conduction band potential of Bi_2S_3 is more negative than that of BiOBr, the valence band potential of Bi_2S_3 is more positive than that of BiOBr. This suitable energy band structure between them is conducive to charge separation and transfer efficiency to enhance photocatalytic performance. However, because the conduction band edge potential of $BiOBr/Bi_2S_3$ is often insufficient to reduce O_2 to superoxide radicals, the efficiency of photocatalytic degradation of organics is reduced. Therefore, it is feasible to introduce CdS having a more negative conduction band edge potential ($E_{CB} \approx -0.52$ eV) to form a ternary compound semiconductor material [20].

A sea urchin-shaped hollow $BiOBr/Bi_2S_3/CdS$ composite material was prepared by directly synthesizing BiOBr microspheres in one pot. The research on the photocatalytic performance of the composite material confirmed the view that the ternary composite material has a better catalytic effect. Those results are of great significance to discuss the photodegradation mechanism of dyes in the presence of $BiOBr/Bi_2S_3/CdS$ composites.

2. Experimental Section

2.1. Materials and Preparation of BiOBr/Bi₂S₃/CdS Composite

The description of the synthesis methods of $BiOBr/Bi_2S_3/CdS$ composite material, the required raw materials, as well as the analytical techniques used for characterization of the materials can be found in the Supplementary Materials.

2.2. Photocatalytic Degradation Studies

In order to study the degradation performance of the synthesized catalyst on methylene blue (MeB), experiments proceeded under a 150 W visible light source halogen lamp, and the light source was 15 cm away from the reaction solution. In a reaction vessel, the prepared photocatalysts (50 mg) were dispersed in MeB solution (10 mg·L^{-1}, 50 mL) and maintained in darkness for 1 h to achieve the adsorption–desorption equilibrium. Then the light source was turned on to initiate the photocatalytic reaction and 3 mL samples were collected from different beakers at the same time intervals. Immediately after filtration, a UV/Vis spectrophotometer was used to record the change in absorbance. Each experiment was performed three times to ensure accuracy. The relationship between dye removal rate and absorbance is calculated by the following formula (Equation (1)):

$$Degradation(\%) = \frac{A_0 - A}{A_0} \times 100\% = \frac{C_0 - C}{C_0} \times 100\% \qquad (1)$$

where A and A_0 are the absorbance of the dye solution at different times and the initial absorbance of the dye solution (mg·L^{-1}), respectively. C and C_0 are the concentration of the dye solution at different times and the initial concentration of the dye solution, respectively.

3. Results and Discussion

3.1. Characterization of BiOBr/Bi₂S₃/CdS Composite Material

XRD was used to explore the crystal phase and composition of the $BiOBr/Bi_2S_3/CdS$ photocatalyst. Figure 1a shows the XRD patterns of pure Bi_2S_3, BiOBr, CdS and composite material $BiOBr/Bi_2S_3/CdS$. Among them, the XRD pattern shape of the Bi_2S_3 is consistent with that of its orthogonal phase [21]. The characteristic diffraction peaks at 2θ = 25.0°,

28.7°, 31.9° and 42.0° correspond to crystal planes (130), (230), (221) and (002). For pure CdS, the characteristic diffraction peaks are located at 24.8°, 26.5°, 28.6°, 43.7° and 52.1°, corresponding to the (100), (002), (101), (110) and (112) crystal planes of the hexagonal structure of CdS. The diffraction peaks of the synthesized pure BiOBr at 2θ values of 10.9°, 25.1°, 31.7°, 32.2°, 46.2°, 50.6°, 53.4° and 56.2° are consistent with the structure of tetragonal BiOBr. The characteristic peaks correspond to (001), (101), (102), (110), (200), (104), (211) and (114), respectively [22]. For the composite $BiOBr/Bi_2S_3/CdS$, its XRD pattern shows the key characteristic peaks of Bi_2S_3 and CdS, indicating that BiOBr is successfully partly vulcanized, while the exposed (001) and (110) crystal planes of the BiOBr microspheres themselves are not covered. The $BiOBr/Bi_2S_3/CdS$ composite prepared using the TAA vulcanization method will not completely change the tetragonal crystal phase of BiOBr [23].
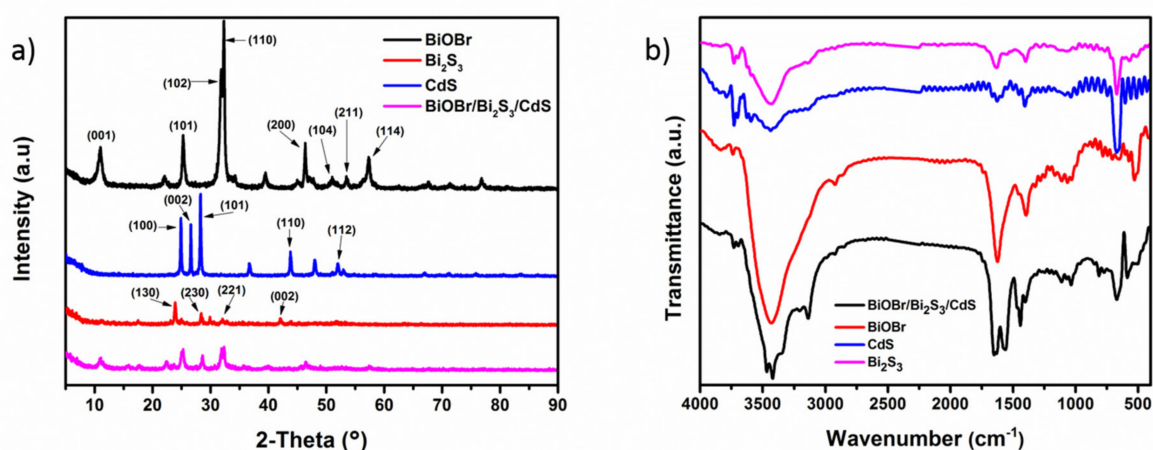

Figure 1. (**a**) XRD patterns of BiOBr, CdS, Bi_2S_3, and $BiOBr/Bi_2S_3/CdS$. (**b**) FT-IR spectra of Bi_2S_3, CdS, BiOBr and $BiOBr/Bi_2S_3/CdS$.

As depicted in Figure 1b, the absorption peak at 606 cm^{-1} is assigned to the characteristic peak of CdS and Bi_2S_3. BiOBr, Bi_2S_3 and CdS samples displayed a similar spectrum and possessed the same peak at about 1400 cm^{-1}, 1630 cm^{-1} and 3400 cm^{-1}. All the characteristic peaks above appeared in $BiOBr/Bi_2S_3/CdS$, indicating that part of BiOBr was successfully vulcanized into Bi_2S_3 and CdS was successfully loaded.

The SEM images of BiOBr, Bi_2S_3 and $BiOBr/Bi_2S_3/CdS$ to determine the morphology of the composite are shown in Figure 2. From Figure 2a, the prepared pure BiOBr has a microsphere structure with an average diameter of 3.5 μm. The partially enlarged view shows that BiOBr microspheres are formed by stacking many BiOBr nanosheet structures. Figure 2b shows the pure Bi_2S_3 with a typical needle-like structure. Figure 2c,d clearly illustrate that the composite $BiOBr/Bi_2S_3/CdS$ has a sea urchin-like structure. The red indicated area is mainly the microsphere structure retained by BiOBr, and some of the microspheres show a cavity structure due to more complete vulcanization. The needle-like structure grown on the microsphere structure is mainly composed of Bi_2S_3 formed by vulcanization and a small amount of CdS. In addition, the irregular surface shape of the microsphere structure is mainly due to the adhesion of CdS nanoparticles on parts of the BiOBr crystal surface [24]. Figure 3 shows the selected area EDS results of the composite $BiOBr/Bi_2S_3/CdS$, where the selected area is the one shown in Figure 2d. The content of the five elements Bi, Cd, Br, S and O in the composite material basically meets the expectations of the composite material, which further confirms the successful preparation of the material.
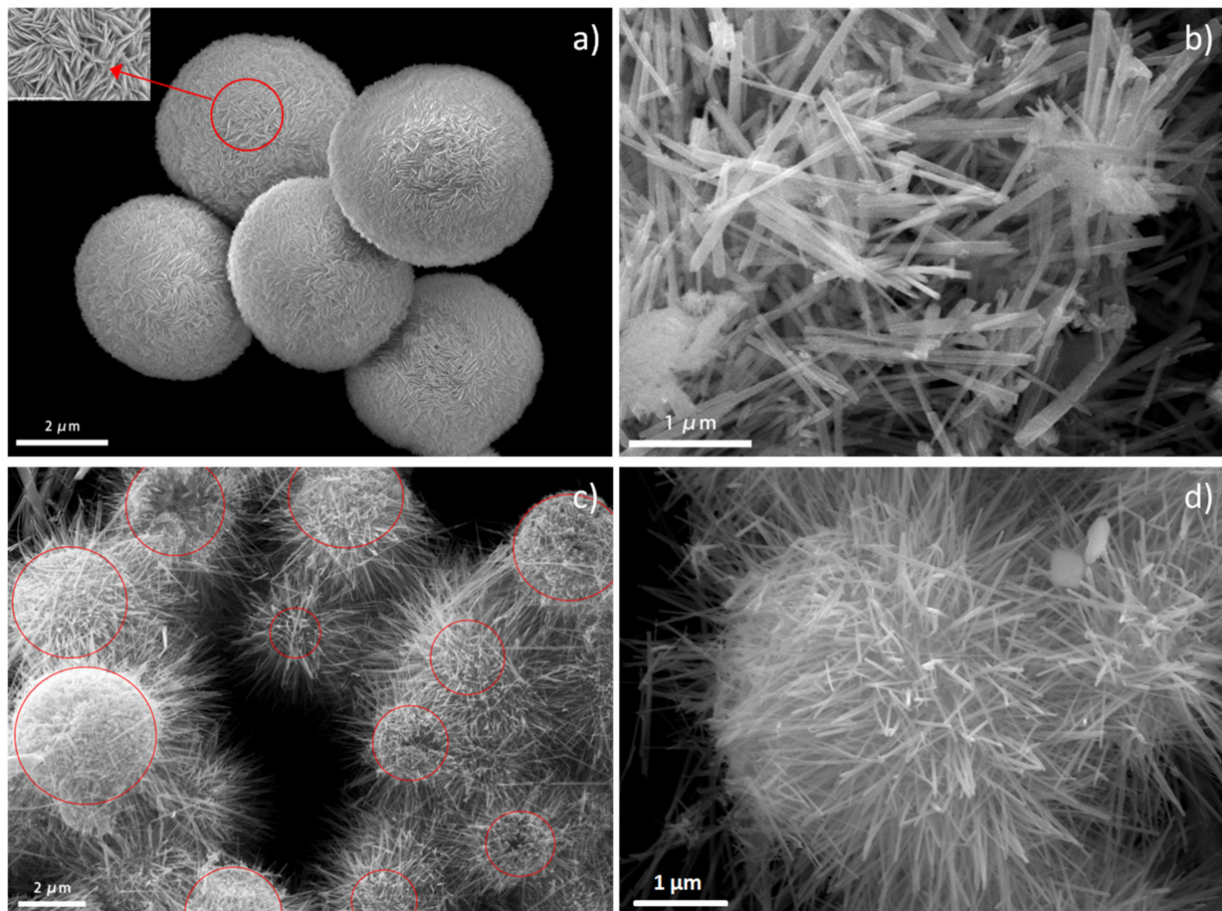
Figure 2. SEM images and partial enlarged images of (**a**) BiOBr, (**b**) Bi_2S_3 and (**c,d**) $BiOBr/Bi_2S_3/CdS$ composite.
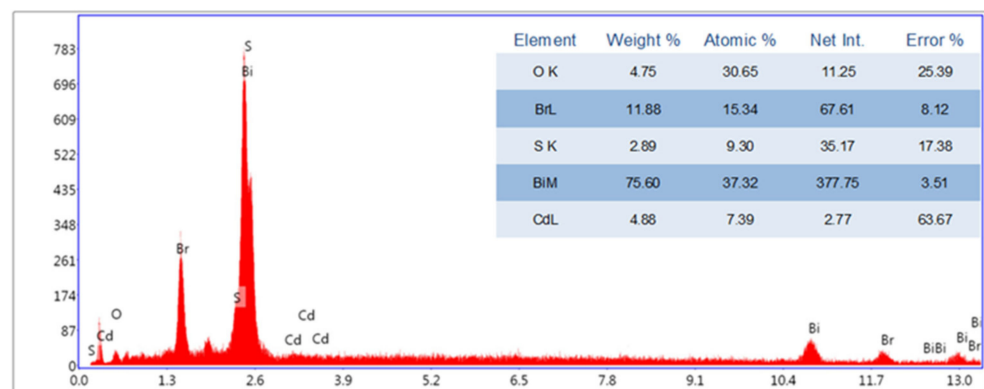

Figure 3. Local EDS results of the $BiOBr/Bi_2S_3/CdS$ composite shown in Figure 2d.

XPS was applied to further analyze the chemical state of the sea urchin-like $BiOBr/Bi_2S_3/CdS$ material, and the results are presented in Figure 4. The full measurement spectrum in Figure 4a shows the strong characteristic peaks of Bi, Cd, O and Br and the weak characteristic peak of S, thus confirming the existence of Bi, Cd, O, Br and S in $BiOBr/Bi_2S_3/CdS$. The peak near the binding energy of 227.6 eV is attributed to S 2s, which indicates the presence of S^{2-} in the complex. The two strong peaks at 164.6 eV and 159.3 eV shown in Figure 4b can be attributed to Bi $4f_{5/2}$ and Bi $4f_{7/2}$ of Bi^{3+} in $BiOBr/Bi_2S_3/CdS$ and the two peaks at 159.2 eV and 161.3 eV can be attributed to S 2p [25,26]. It was confirmed that the precursor BiOBr was sulfided to form Bi_2S_3, a trivalent sulfide of Bi. The strong peaks at the binding energy of 68.3 eV and 69.3 eV shown in Figure 4c belong to the Br $3d_{5/2}$ and Br $3d_{3/2}$ orbital, which is consistent with the XPS results of Br in the

BiOBr report in the literature [27]. The Cd 3d orbital in Figure 4d shows the electronic binding energy of Cd $3d_{5/2}$ at 405.05 eV and 411.7 eV. The characteristic peaks at these two positions have been proved to belong to CdS [20]. It shows that there is Cd^{2+} sulfide CdS in the composite material. The above XPS results verify that the composition and valence of each component of sea urchin-like $BiOBr/Bi_2S_3/CdS$ are in line with expectations.
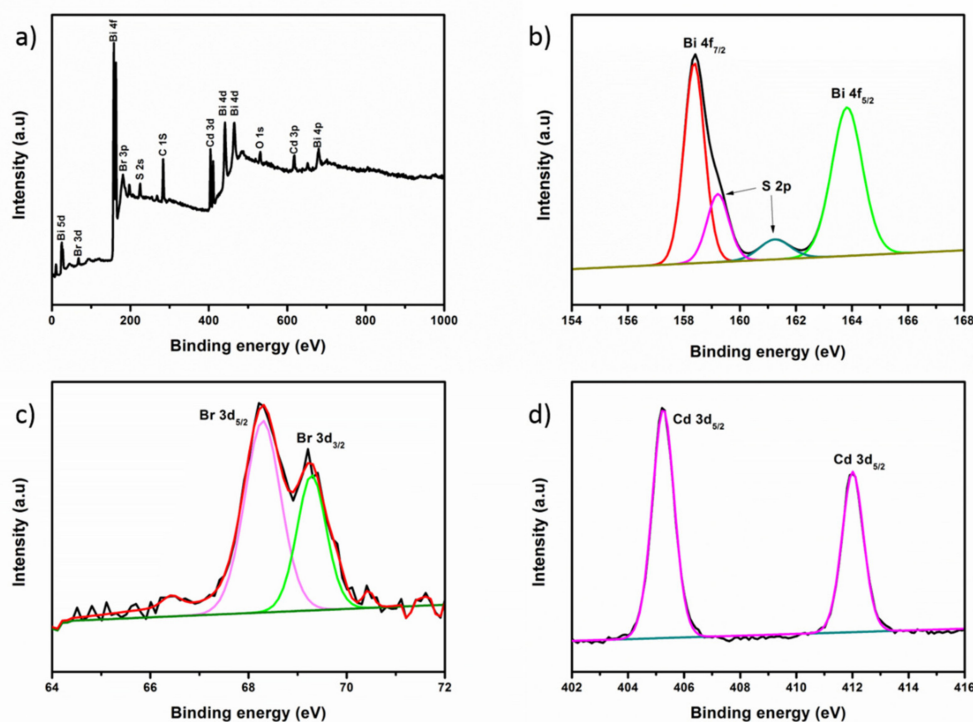
Figure 4. XPS spectra of $BiOBr/Bi_2S_3/CdS$: (**a**) full spectrum, (**b**) Bi 4f, (**c**) Br 3d, (**d**) Cd 3d.

3.2. Photocatalytic Performance

The photocatalytic activity of the $BiOBr/Bi_2S_3/CdS$ composite material was evaluated by degrading MeB solution under an indoor metal halide lamp. Figure 5 shows the experimental results of visible light catalytic removal of MeB in the presence of pure BiOBr, Bi_2S_3, CdS and $BiOBr/Bi_2S_3/CdS$ complexes. MeB is usually relatively stable under the irradiation of metal halide lamps, so the self-photolysis effect is negligible. Dark treatment showed that pure BiOBr, Bi_2S_3, CdS and $BiOBr/Bi_2S_3/CdS$ composite materials had a certain adsorption capacity, especially BiOBr spheres with a large specific surface area have a strong adsorption effect on MeB dye and almost reach equilibrium within 60 min. The efficient adsorption of BiOBr for dyes was similar to other researches [28]. After 120 min of subsequent exposure to the metal halide lamp, pure Bi_2S_3, CdS and $BiOBr/Bi_2S_3/CdS$ all produced a certain degree of removal performance for MeB. Among them, the $BiOBr/Bi_2S_3/CdS$ composite photocatalyst can achieve 83.3% degradation efficiency of MeB dye. This showed that $BiOBr/Bi_2S_3/CdS$ composite material can efficiently remove MeB dye contaminants under visible light.
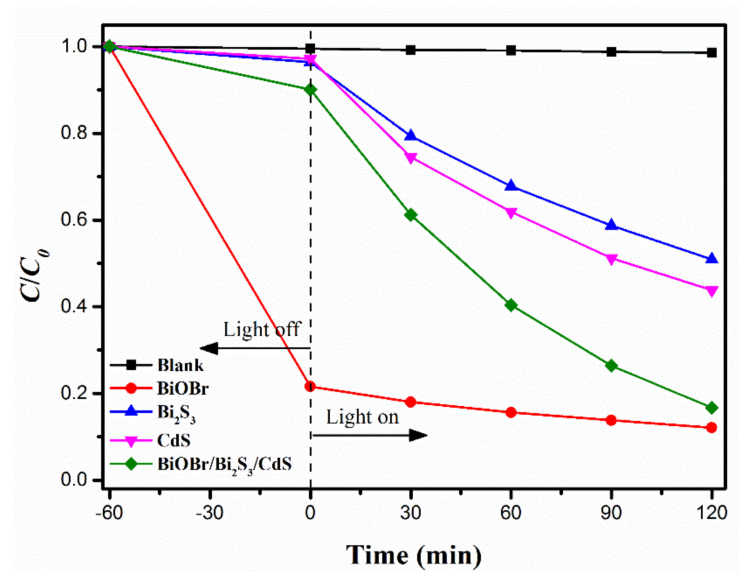
Figure 5. Effect of different catalysts on photocatalytic degradation of MeB.

Subsequently, in order to evaluate the photocatalytic activity of the composite catalyst, the Langmuir–Hinshelwood (L-H) equation was used to fit the reaction kinetics. The results show that the photocatalytic reaction follows the following pseudo-first-order kinetic model (Equation (2)) [29]:

$$ln\frac{C_0}{C} = kt \tag{2}$$

where C_0 and C are the initial concentration of the dye solution and the concentration of the dye solution at different times, k and t are the rate constants of the system and the time. The result is shown in Figure 6. The degradation of MeB by each material follows a pseudo-first-order kinetic model, and BiOBr/Bi$_2$S$_3$/CdS has the largest reaction rate. Table 1 contains the rate constants and correlation coefficients of the pseudo-first-order kinetics of each photocatalyst. It can be seen that compared to the original BiOBr, Bi$_2$S$_3$ and CdS photocatalysts, the reaction rate of the BiOBr/Bi$_2$S$_3$/CdS composite for MeB degradation has increased by 1.96, 1.67 and 1.14 times, respectively.
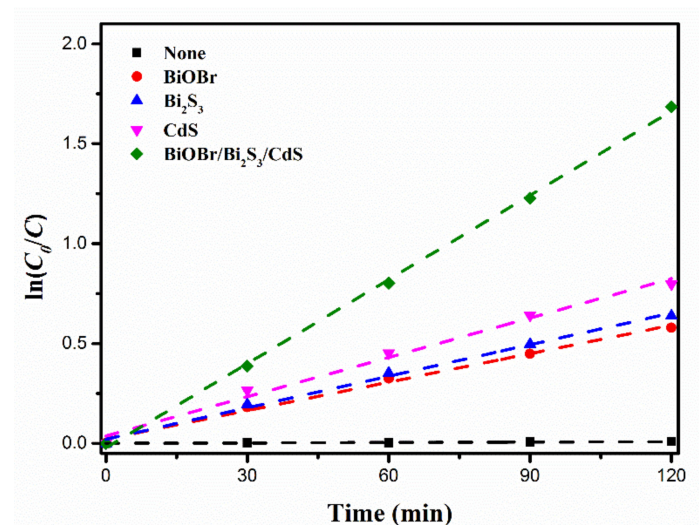

Figure 6. The pseudo-first-order kinetics degradation of MeB in the presence of different catalysts.

Table 1. Rate constants and correlation coefficients of MeB photocatalytic degradation by BiOBr, Bi_2S_3, CdS and $BiOBr/Bi_2S_3/CdS$.

Catalyst	k (min^{-1})	(R^2)
BiOBr	0.00475	0.9916
Bi_2S_3	0.00526	0.9941
CdS	0.00656	0.9872
$BiOBr/Bi_2S_3/CdS$	0.01404	0.9987

3.3. Cycling Experiments

Five continuous degradation cycles in presence of $BiOBr/Bi_2S_3/CdS$ composite photocatalyst were studied. As shown in Figure 7, after the fifth cycle the degradation efficiency of MeB remained at about 78.4% and the catalytic efficiency of the catalyst decreased by only 4.9%. This indicates that the sea urchin-like $BiOBr/Bi_2S_3/CdS$ composite has excellent stability under the MeB degradation.
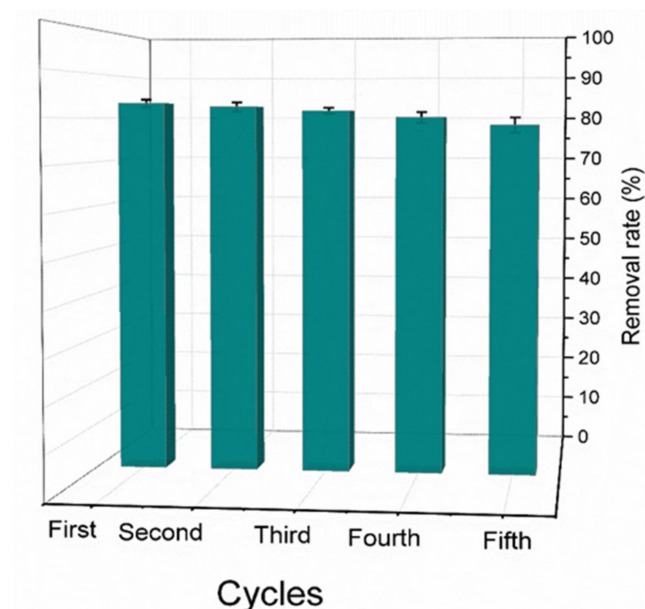

Figure 7. Recycling performance of photocatalytic degradation of MeB by $BiOBr/Bi_2S_3/CdS$ composite under visible light illumination.

3.4. Exploration of Photocatalytic Reaction Mechanism

The optical properties of pure BiOBr, Bi_2S_3, CdS and $BiOBr/Bi_2S_3/CdS$ composite materials were verified by UV-Vis, and the results are shown in Figure 8. It can be seen that pure BiOBr has a small amount of absorption at the edge of the visible light region, while CdS can absorb light in a larger range than BiOBr. Bi_2S_3 is different from them, its absorption range covers the entire ultraviolet and visible light regions. Studies have shown that as the vulcanization duration increases, the absorption edge of the composite material formed by BiOBr gradually shifts to a longer wavelength, which indicates that the introduced Bi_2S_3 has a strong visible light response [30]. Therefore, the absorption edge of the $BiOBr/Bi_2S_3/CdS$ composite shifts to higher wavelengths, and it also exhibits a certain intensity of absorption of visible light at higher wavelengths. This fully shows that the introduction of Bi_2S_3 and CdS increases the visible light utilization rate of the original BiOBr, thereby improving its photocatalytic efficiency. Subsequently, in order to more accurately understand the changes in the light absorption characteristics after

recombination, the band gap energy E_g of each substance was calculated using the intercept method. The calculation formula of E_g is as follows (Equation (3)) [31]:

$$Eg = \frac{1240}{\lambda_g} \tag{3}$$
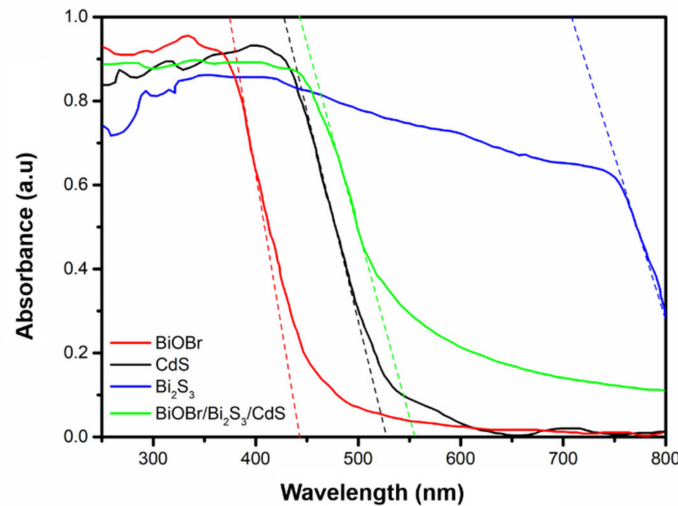
Figure 8. UV/Vis spectra of BiOBr, Bi_2S_3, CdS and the BiOBr/Bi_2S_3/CdS composite.

The band edge wavelength (λ_g) is determined by extrapolating the sharply rising part of the curve to the abscissa at zero absorption (dashed lines in Figure 8). The band gaps of pure BiOBr, Bi_2S_3, CdS and BiOBr/Bi_2S_3/CdS composites were estimated. The results showed that the band gap widths of BiOBr, Bi_2S_3, CdS and BiOBr/Bi_2S_3/CdS were 2.81 eV, 1.46 eV, 2.36 eV and 2.23 eV, respectively. This shows that the band gap energy of the composite decreases with the sulfidation of BiOBr and the addition of sulfide, which will help to enhance the photocatalytic performance of the composite.

Some reactive species, including holes (h^+), photo-generated electrons (e^-), superoxide radical anions ($\bullet O_2^-$) and hydroxyl radicals ($\bullet OH$), have successfully separated the degradation of organic pollutants after generating photogenerated charge carriers on the surface of light and photocatalyst [32]. In order to reveal the reactive species in the process of dye degradation, trap-trap experiments were carried out with 1 mM tert-butyl alcohol (TBA), p-benzoquinone (p-BQ), ammonium oxalate (AO) and potassium bromate (PB). TBA, P-BQ, AO and PB were used to capture $\bullet OH$, $\bullet O_2^-$, h^+ and e^-, respectively [33,34]. Figure 9 shows the changes in MeB degradation in the presence of various scavengers. After the introduction of p-BQ and AO, the two-hour removal rate dropped visibly. However, the effect of introducing TBA and PB on the removal of MeB by the catalyst is negligible (close to blank). These results indicate that the superoxide radical $\bullet O_2^-$ and h^+ are the main substances produced by BiOBr/Bi_2S_3/CdS under visible light, and they subsequently degrade MeB. To verify the experimental results of free radical generation, EPR spin trapping was used [35]. The result is shown in Figure 10. Under visible light, the use of BiOBr/Bi_2S_3/CdS catalyst to degrade MeB was recorded with a strong DMPO-$\bullet O_2^-$ signal. This proves that in addition to the known h^+, the composite catalyst can also produce $\bullet O_2^-$ as a reactive substance under visible light.
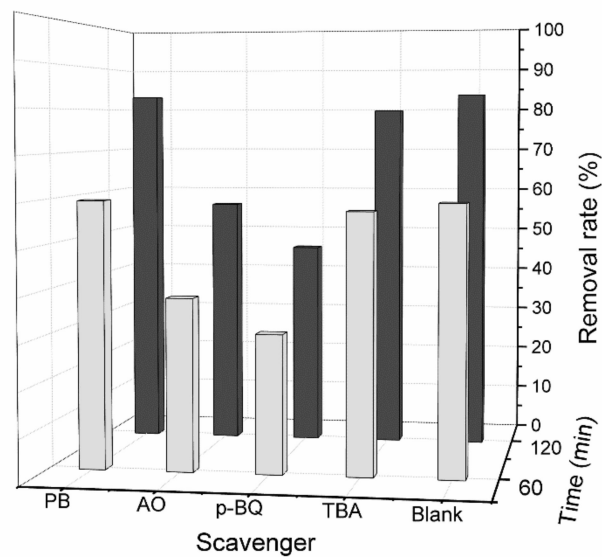
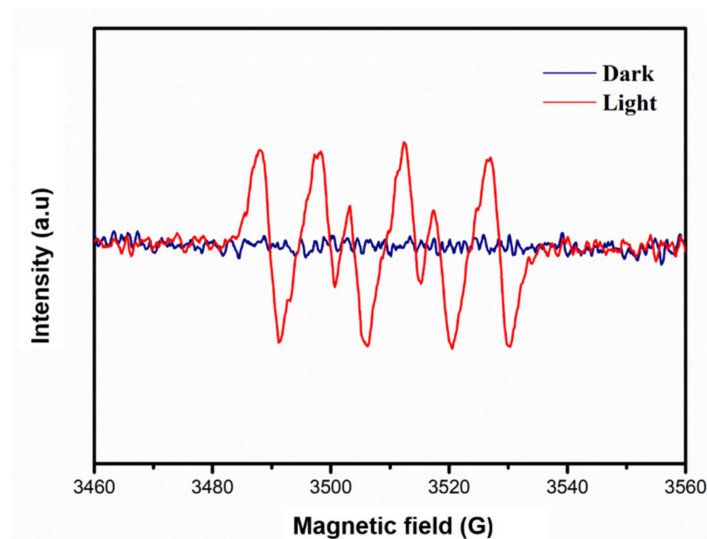**Figure 9.** Photocatalytic degradation of MeB by $BiOBr/Bi_2S_3/CdS$ in presence of different scavengers.

Figure 10. DMPO spin-trapping EPR spectra of $\bullet O_2{}^-$ in MeB solution under dark conditions and visible light irradiation.

Based on the results of the active species studies discussed above, a possible photocatalytic degradation mechanism is proposed by determining the edge potential of the valence band (VB) and conduction band (CB) of BiOBr, Bi_2S_3 and CdS, and it is illustrated schematically in Figure 11. The VB and CB potentials of BiOBr, Bi_2S_3 and CdS can be calculated using the following formula (Equations (4) and (5)) [36]:

$$E_{VB} = X - E^e + 0.5E_g \tag{4}$$

$$E_{CB} = E_{VB} - E_g \tag{5}$$

where E_{VB} and E_{CB} are the edge potentials of the valence band and conduction band, E^e is the energy of free electrons on the hydrogen scale (about 4.5 eV), and X is the semiconductor electronegativity of BiOBr, Bi_2S_3 and CdS, which are 6.18 eV, 5.35 eV and 5.16 eV, respectively. Using the band gap energies of BiOBr, Bi_2S_3 and CdS being 2.81 eV, 1.46 eV, and 2.36 eV, respectively, the VB and CB potentials of BiOBr were calculated to be 3.09 eV and 0.28 eV, the VB and CB potentials of Bi_2S_3 are 1.58 eV and 0.12 eV, and the VB and CB potentials of CdS were calculated to be 1.84 eV and -0.52 eV.
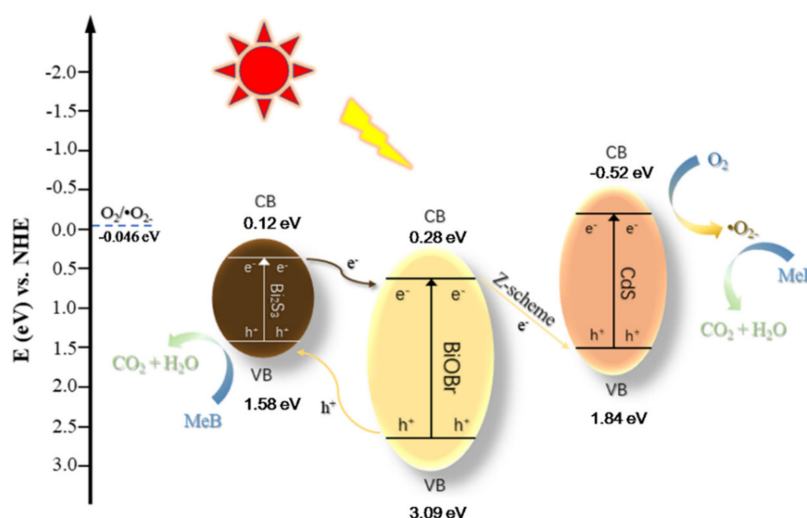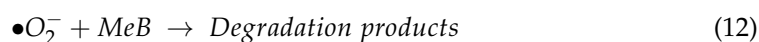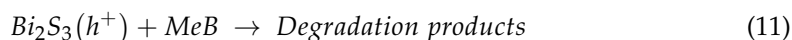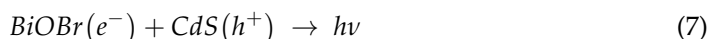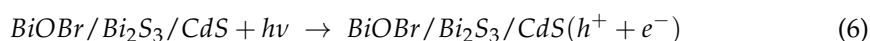
Figure 11. Proposed mechanisms for photocatalytic degradation of MeB by $BiOBr/Bi_2S_3/CdS$.

Since BiOBr is a p-type semiconductor, its Fermi level is close to its valence band, while CdS and Bi_2S_3 are n-type semiconductors, and its Fermi level is close to its conduction band. Therefore, the contact between the semiconductors and the balance of the Fermi level lead to the formation of p-n heterojunctions. This can be achieved by the upward shift of the Fermi level of BiOBr and the downward shift of the Fermi level of CdS and Bi_2S_3. The balance of the Fermi energy level causes the VB and CB of CdS and Bi_2S_3 to move positively, while the VB and CB of BiOBr move negatively. BiOBr, Bi_2S_3 and CdS are all visible active photocatalysts. Therefore, continuous visible light irradiation of the $BiOBr/Bi_2S_3/CdS$ composite causes BiOBr, Bi_2S_3 and CdS to form charge carriers. However, because the VB of BiOBr is in a more positive position than the VB of Bi_2S_3, the holes in the VB of Bi_2S_3 degrade MeB, while the electrons on the CB of Bi_2S_3 transfer to the CB of BiOBr, hindering its reorganization. On the other hand, the width of the CB of CdS makes the electron light excited to a higher CB, and the annihilation of the h^+ on the VB of CdS and the electron (e^-) on the CB of BiOBr on the conductive medium also reduces the recombination, and the CB of CdS. The e^- at the place reacts with O_2 to generate $\bullet O_2^-$ for further degradation of MeB [37]. In addition, because the CB of BiOBr and Bi_2S_3 cannot reach the formation potential E_0 of $\bullet O_2^-$ ($O_2/\bullet O_2^- = -0.046$ eV), the recombination of CdS with a more negative CB plays a key role in the generation of superoxide radicals. In summary, the photo-induced carrier transfer process and MeB removal process at each stage of the photocatalytic process are shown in formula (Equations (6)–(12)) [38]:

$$BiOBr/Bi_2S_3/CdS + hv \;\rightarrow\; BiOBr/Bi_2S_3/CdS(h^+ + e^-) \tag{6}$$

$$BiOBr(e^-) + CdS(h^+) \;\rightarrow\; hv \tag{7}$$

$$BiOBr(h^+) \;\rightarrow\; Bi_2S_3(h^+) \tag{8}$$

$$Bi_2S_3(e^-) \;\rightarrow\; BiOBr(e^-) \tag{9}$$

$$O_2 + CdS(e^-) \;\rightarrow\; \bullet O_2^- \tag{10}$$

$$Bi_2S_3(h^+) + MeB \;\rightarrow\; Degradation\ products \tag{11}$$

$$\bullet O_2^- + MeB \;\rightarrow\; Degradation\ products \tag{12}$$

4. Conclusions

BiOBr microspheres were synthesized first in this work, and a $BiOBr/Bi_2S_3/CdS$ composite with a sea urchin-like shape was directly obtained by the one-pot method. The morphology, structure and composition of the composite material were fully characterized

by XRD, FT-IR, SEM, EDS and XPS. When the initial concentration of MeB aqueous solution is 10 mg·L^{-1}, pH = 7, catalyst dosage 50 mg and the reaction temperature at 30 °C, the best visible light catalytic efficiency can be achieved, and the two-hour removal rate of MeB reaches 83.3%. The MeB photocatalytic degradation process followed a pseudo-first-order kinetic model, and the reaction rate under optimal conditions is 0.014 min^{-1}, which is 1.1, 1.7 and two times higher than that of pure CdS, Bi_2S_3 and BiOBr, respectively. The results of the cycling experiment showed that the degradation rate of MeB under the optimal conditions only decreased by 4.9%for the $BiOBr/Bi_2S_3/CdS$ composite after five cycles, which confirmed the material has good stability. The band gap energy of $BiOBr/Bi_2S_3/CdS$ was calculated to be 2.23 eV from the ultraviolet/visible diffuse reflectance spectrum. •O_2^- and h$^+$ were the main active species involved in the photocatalytic degradation of MeB through quenching experiment and EPR test results, which explained the reaction mechanism and confirmed the key role of CdS in the production of •O_2^-. The analysis of the above results proved that the sea urchin-like $BiOBr/Bi_2S_3/CdS$, as a semiconductor composite material with a moderate band gap, is expected to show more applications in the field of photocatalysis.

Symbols

A	absorbance of the dye solution [-]
A_0	initial absorbance of the dye solution [-]
C	concentration of the dye solution [mol L^{-1}]
C_0	initial concentration of the dye solution [mol L^{-1}]
E_0	formation potential of $O_2{}^-$ [eV]
E_g	band gap energy [eV]
E_{CB}	edge potentials of conduction band [eV]
E_{VB}	edge potentials of the valence band [eV]
E^e	energy of free electrons on the hydrogen scale [eV]
K	rate constant [min^{-1}]
t	reaction time [min]
R^2	correlation coefficient [-]
X	electronegativity of BiOBr, Bi_2S_3 and CdS [eV]
Greek letters	
Λ_g	band edge wavelength [m]
Abbreviations	
AO	ammonium oxalate
CB	conduction band
PB	potassium bromate
p-BQ	p-benzoquinone
TAA	thioacetamide
TBA	tert-butanol
VB	valence band

References

1. Chiam, S.L.; Pung, S.Y.; Yeoh, F.Y. Recent developments in MnO_2-based photocatalysts for organic dye removal: A review. *Environ. Sci. Pollut. Res.* **2020**, *27*, 5759–5778. [CrossRef]
2. Lin, S.; Song, Z.L.; Che, G.B.; Ren, A.; Li, P.; Liu, C.B.; Zhang, J.H. Adsorption behavior of metal-organic frameworks for methylene blue from aqueous solution. *Microporous Mesoporous Mat.* **2014**, *193*, 27–34. [CrossRef]
3. Chen, S.H.; Zhang, J.; Zhang, C.L.; Yue, Q.Y.; Li, Y.; Li, C. Equilibrium and kinetic studies of methyl orange and methyl violet adsorption on activated carbon derived from Phragmites australis. *Desalination* **2010**, *252*, 149–156. [CrossRef]
4. Wang, S.B.; Boyjoo, Y.; Choueib, A.; Zhu, Z.H. Removal of dyes from aqueous solution using fly ash and red mud. *Water Res.* **2005**, *39*, 129–138. [CrossRef] [PubMed]
5. Islam, M.A.; Ali, I.; Karim, S.M.A.; Firoz, M.S.H.; Chowdhury, A.; Morton, D.W.; Angove, M.J. Removal of dye from polluted water using novel nano manganese oxide-based materials. *J. Water Process. Eng.* **2019**, *32*, 21. [CrossRef]
6. Ranjith, R.; Renganathan, V.; Chen, S.-M.; Selvan, N.S.; Rajam, P.S. Green synthesis of reduced graphene oxide supported TiO_2/Co_3O_4 nanocomposite for photocatalytic degradation of methylene blue and crystal violet. *Ceram. Int.* **2019**, *45*, 12926–12933. [CrossRef]
7. Liu, J.; Wang, D.; Wang, M.; Kong, D.; Zhang, Y.; Chen, J.F.; Dai, L. Uniform Two-Dimensional Co_3O_4 Porous Sheets: Facile Synthesis and Enhanced Photocatalytic Performance. *Chem. Eng. Technol.* **2016**, *39*, 891–898. [CrossRef]
8. Crini, G. Non-conventional low-cost adsorbents for dye removal: A review. *Bioresour. Technol.* **2006**, *97*, 1061–1085. [CrossRef] [PubMed]
9. Ran, J.; Zhang, J.; Yu, J.; Jaroniec, M.; Qiao, S.Z. Earth-abundant cocatalysts for semiconductor-based photocatalytic water splitting. *Chem. Soc. Rev.* **2014**, *43*, 7787–7812. [CrossRef]
10. Baniamerian, H.; Teimoori, M.; Saberi, M. Fe_2O_3/TiO_2/Activated Carbon Nanocomposite with Synergistic Effect of Adsorption and Photocatalysis. *Chem. Eng. Technol.* **2021**, *44*, 130–139. [CrossRef]
11. Truong, D.H.; Vo, V.; Van Gerven, T.; Leblebici, M.E. A Facile Method for the Synthesis of a MoS_2/g-C_3N_4. Photocatalyst. *Chem. Eng. Technol.* **2019**, *42*, 2691–2699. [CrossRef]
12. Yan, P.; Jiang, D.; Tian, Y.; Xu, L.; Qian, J.; Li, H.; Xia, J.; Li, H. A sensitive signal-on photoelectrochemical sensor for tetracycline determination using visible-light-driven flower-like CN/BiOBr composites. *Biosens. Bioelectron.* **2018**, *111*, 74–81. [CrossRef] [PubMed]
13. Xia, J.X.; Di, J.; Li, H.T.; Xu, H.; Li, H.M.; Guo, S.J. Ionic liquid-induced strategy for carbon quantum dots/BiOX (X = Br, Cl) hybrid nanosheets with superior visible light-driven photocatalysis. *Appl. Catal. B-Environ.* **2016**, *181*, 260–269. [CrossRef]
14. Shenoy, S.; Sridharan, K. Bismuth oxybromide nanoplates embedded on activated charcoal as effective visible light driven photocatalyst. *Chem. Phys. Lett.* **2020**, *749*, 137435. [CrossRef]
15. Sridharan, K.; Shenoy, S.; Kumar, S.G.; Terashima, C.; Fujishima, A.; Pitchaimuthu, S. Advanced Two-Dimensional Heterojunction Photocatalysts of Stoichiometric and Non-Stoichiometric Bismuth Oxyhalides with Graphitic Carbon Nitride for Sustainable Energy and Environmental Applications. *Catalysts* **2021**, *11*, 426. [CrossRef]

16.   Di, T.; Xu, Q.; Ho, W.; Tang, H.; Xiang, Q.; Yu, J. Review on Metal Sulphide-based Z-scheme Photocatalysts. *ChemCatChem* **2019**, *11*, 1394–1411. [CrossRef]

17.   Guan, S.; Yang, H.; Sun, X.; Xian, T. Preparation and promising application of novel LaFeO$_3$/BiOBr heterojunction photocatalysts for photocatalytic and photo-Fenton removal of dyes. *Opt. Mater.* **2020**, *100*, 109644. [CrossRef]

18.   Yang, Z.; Tong, X.; Feng, J.; He, S.; Fu, M.; Niu, X.; Zhang, T.; Liang, H.; Ding, A.; Feng, X. Flower-like BiOBr/UiO-66-NH$_2$ nanosphere with improved photocatalytic property for norfloxacin removal. *Chemosphere* **2019**, *220*, 98–106. [CrossRef]

19.   Wang, W.N.; Zhang, C.Y.; Zhang, M.F.; Pei, P.; Zhou, W.; Zha, Z.B.; Shao, M.; Qian, H.-S. Precisely photothermal controlled releasing of antibacterial agent from Bi$_2$S$_3$ hollow microspheres triggered by NIR light for water sterilization. *Chem. Eng. J.* **2020**, *381*, 122630. [CrossRef]

20.   Yang, M.; Shi, Y.; Li, Y.; Li, H.; Luo, N.; Li, J.; Fan, J.; Zhou, A. Construction of 2D Bi$_2$S$_3$/CdS Nanosheet Arrays for Enhanced Photoelectrochemical Hydrogen Evolution. *J. Electron. Mater.* **2019**, *48*, 6397–6405. [CrossRef]

21.   Liang, Q.; Ploychompoo, S.; Chen, J.; Zhou, T.; Luo, H. Simultaneous Cr(VI) reduction and bisphenol A degradation by a 3D Z-scheme Bi$_2$S$_3$-BiVO$_4$ graphene aerogel under visible light. *Chem. Eng. J.* **2020**, *384*, 123256. [CrossRef]

22.   Shi, X.J.; Chen, X.; Chen, X.L.; Zhou, S.M.; Lou, S.Y.; Wang, Y.Q.; Yuan, L. PVP assisted hydrothermal synthesis of BiOBr hierarchical nanostructures and high photocatalytic capacity. *Chem. Eng. J.* **2013**, *222*, 120–127. [CrossRef]

23.   Deng, W.; Pan, F.P.; Batchelor, B.; Jung, B.M.; Zhang, P.; Abdel-Wahab, A.; Zhou, H.C.; Li, Y. Mesoporous TiO$_2$-BiOBr microspheres with tailorable adsorption capacities for photodegradation of organic water pollutants: Probing adsorption-photocatalysis synergy by combining experiments and kinetic modeling. *Environ. Sci. Wat. Res. Technol.* **2019**, *5*, 769–781. [CrossRef]

24.   Cui, W.; An, W.; Liu, L.; Hu, J.; Liang, Y. Synthesis of CdS/BiOBr composite and its enhanced photocatalytic degradation for Rhodamine B. *Appl. Surf. Sci.* **2014**, *319*, 298–305. [CrossRef]

25.   Qiu, J.; Wu, M.; Yu, L.; Li, J.; Di, J.; Zhang, S.; Luo, Z.; Zhang, S.; Li, Z.; Wu, Z. Vanadate-Rich BiOBr/Bi Nanosheets for Effective Adsorption and Visible-Light-Driven Photodegradation of Rhodamine B. *J. Nanosci. Nanotechnol.* **2020**, *20*, 2267–2276. [CrossRef] [PubMed]

26.   Wang, Y.H.; Kang, C.L.; Xiao, K.K.; Wang, X.Y. Fabrication of Bi$_2$S$_3$/MOFs composites without noble metals for enhanced photoreduction of Cr (VI). *Sep. Purif. Technol.* **2020**, *241*, 8. [CrossRef]

27.   Imam, S.S.; Adnan, R.; Mohd Kaus, N.H. Room-temperature synthesis of flower-like BiOBr/Bi$_2$S$_3$ composites for the catalytic degradation of fluoroquinolones using indoor fluorescent light illumination. *Colloids Surf. A* **2020**, *585*, 124069. [CrossRef]

28.   Wu, S.; Xie, Y.; Zhang, X.; Huang, Z.; Liu, Y.; Fang, M.; Wu, X.; Min, X. In situ synthesis of adsorptive β-Bi$_2$O$_3$/BiOBr photocatalyst with enhanced degradation efficiency. *J. Mater. Res.* **2019**, *34*, 3450–3461. [CrossRef]

29.   Hassan, N.S.; Jalil, A.A.; Khusnun, N.F.; Ali, M.W.; Haron, S. Role of reduced graphene oxide in improving interfacial charge transfer of hybridized rGO/silica/zirconia for enhanced Bisphenol A photodegradation. *J. Alloys Compd.* **2019**, *789*, 221–230. [CrossRef]

30.   Cui, Y.; Jia, Q.; Li, H.; Han, J.; Zhu, L.; Li, S.; Zou, Y.; Yang, J. Photocatalytic activities of Bi$_2$S$_3$/BiOBr nanocomposites synthesized by a facile hydrothermal process. *Appl. Surf. Sci.* **2014**, *290*, 233–239. [CrossRef]

31.   Xu, Z.; Yu, Y.; Fang, D.; Liang, J.; Zhou, L. Simulated solarlight catalytic reduction of Cr(VI) on microwave–ultrasonication synthesized flower-like CuO in the presence of tartaric acid. *Mater. Chem. Phys.* **2016**, *171*, 386–393. [CrossRef]

32.   Shenoy, S.; Ahmed, S.; Lo, I.M.C.; Singh, S.; Sridharan, K. Rapid sonochemical synthesis of copper doped ZnO grafted on graphene as a multi-component hierarchically structured visible-light-driven photocatalyst. *Mater. Res. Bull.* **2021**, *140*, 111290. [CrossRef]

33.   Khampuanbut, A.; Santalelat, S.; Pankiew, A.; Channei, D.; Pornsuwan, S.; Faungnawakij, K.; Phanichphant, S.; Inceesungvorn, B. Visible-light-driven WO$_3$/BiOBr heterojunction photocatalysts for oxidative coupling of amines to imines: Energy band alignment and mechanistic insight. *J. Colloid Interface Sci.* **2020**, *560*, 213–224. [CrossRef]

34.   Shenoy, S.; Jang, E.; Park, T.J.; Gopinath, C.S.; Sridharan, K. Cadmium sulfide nanostructures: Influence of morphology on the photocatalytic degradation of erioglaucine and hydrogen generation. *Appl. Surf. Sci.* **2019**, *483*, 696–705. [CrossRef]

35.   Kumar, A.; Sharma, S.K.; Sharma, G.; Al-Muhtaseb, A.H.; Naushad, M.; Ghfar, A.A.; Stadler, F.J. Wide spectral degradation of Norfloxacin by Ag@BiPO$_4$/BiOBr/BiFeO$_3$ nano-assembly: Elucidating the photocatalytic mechanism under different light sources. *J. Hazard. Mater.* **2019**, *364*, 429–440. [CrossRef] [PubMed]

36.   Shao, B.; Liu, X.; Liu, Z.; Zeng, G.; Liang, Q.; Liang, C.; Cheng, Y.; Zhang, W.; Liu, Y.; Gong, S. A novel double Z-scheme photocatalyst Ag$_3$PO$_4$/Bi$_2$S$_3$/Bi$_2$O$_3$ with enhanced visible-light photocatalytic performance for antibiotic degradation. *Chem. Eng. J.* **2019**, *368*, 730–745. [CrossRef]

37.   Dong, X.A.; Zhang, W.; Sun, Y.; Li, J.; Cen, W.; Cui, Z.; Huang, H.; Dong, F. Visible-light-induced charge transfer pathway and photocatalysis mechanism on Bi semimetal@defective BiOBr hierarchical microspheres. *J. Catal.* **2018**, *357*, 41–50. [CrossRef]

38.   Zhu, S.R.; Qi, Q.; Zhao, W.N.; Fang, Y.; Han, L. Enhanced photocatalytic activity in hybrid composite combined BiOBr nanosheets and Bi$_2$S$_3$ nanoparticles. *J. Phys. Chem. Solids* **2018**, *121*, 163–171. [CrossRef]